HHS Public Access

Author manuscript

Mater Today (Kidlington). Author manuscript; available in PMC 2022 May 01.

Published in final edited form as:

Mater Today (Kidlington). 2021 May ; 45: 20–34. doi:10.1016/j.mattod.2020.11.021.

3D Printing in alloy design to improve biocompatibility in metallic implants

Indranath Mitra[a], **Susmita Bose**[a], **William S. Dernell**[b], **Nairanjana Dasgupta**[c], **Chrissy Eckstrand**[b], **Jim Herrick**[d], **Michael J. Yaszemski**[d], **Stuart B. Goodman**[e], **Amit Bandyopadhyay**[a,*]

[a]W. M. Keck Biomedical Materials Research Laboratory, School of Mechanical and Materials Engineering, Washington State University, Pullman, WA 99164 2920, USA

[b]College of Veterinary Medicine, Washington State University, Pullman, WA 99164, USA

[c]Department of Mathematics and Statistics, Washington State University, Pullman, WA 99164, USA

[d]Department of Orthopedic Surgery, Mayo Clinic, Rochester, MN, USA

[e]Department of Orthopedic Surgery, Stanford University Medical Center, Redwood City, CA 94063, USA

Abstract

3D Printing (3DP) or additive manufacturing (AM) enables parts with complex shapes, design flexibility, and customization opportunities for defect specific patient-matched implants. 3DP or AM also offers a design platform that can be used to innovate novel alloys for application-specific compositional modifications. In medical applications, the biological response from a host tissue depends on a biomaterial's structural and compositional properties in the physiological environment. Application of 3DP can pave the way towards manufacturing innovative metallic implants, combining structural variations at different length scales and tailored compositions designed for specific biological responses. This study shows how 3DP can be used to design metallic alloys for orthopedic and dental applications with improved biocompatibility using *in vitro* and *in vivo* studies. Titanium (Ti) and its alloys are used extensively in biomedical devices due to excellent fatigue and corrosion resistance and good strength to weight ratio. However, Ti

*Corresponding author. Bandyopadhyay, A. (amitband@wsu.edu).

CRediT authorship contribution statement

Indranath Mitra: Investigation, Data curation, Writing - original draft. **Susmita Bose:** Conceptualization, Supervision, Funding acquisition, Writing - review & editing. **William Dernell:** Investigation. **Nairanjana Dasgupta:** Investigation. **Chrissy Eckstrand:** Investigation. **Jim Herrick:** Investigation. **Michael J. Yaszemski:** Investigation. **Stuart B. Goodman:** Investigation. **Amit Bandyopadhyay:** Conceptualization, Supervision, Funding acquisition, Writing - original draft, Writing - review & editing.

Data availability statement

All raw data for this study has been presented in this manuscript.

Conflict of interest

None.

Declaration of Competing Interest

The authors declare that they have no known competing financial interests or personal relationships that could have appeared to influence the work reported in this paper.

Appendix A. Supplementary data

Supplementary data to this article can be found online at https://doi.org/10.1016/j.mattod.2020.11.021.

alloys' *in vivo* biological response is poor due to its bioinert surface. Different coatings and surface modification techniques are currently being used to improve the biocompatibility of Ti implants. We focused our efforts on improving Ti's biocompatibility via a combination of tantalum (Ta) chemistry in Ti, the addition of designed micro-porosity, and nanoscale surface modification to enhance both *in vitro* cytocompatibility and early stage *in vivo* osseointegration, which was studied in rat and rabbit distal femur models.

Introduction

Over 50% of commercial biomedical devices are made of metallic materials primarily used in orthopedic, dental, fracture management, and cardiovascular applications [1]. The reason behind such demand for biomaterials from the bone health point of view is – (1) an increase in the median age of our population, (2) a more active lifestyle, and (3) a change in food habits - as all of these factors contribute to bone health. Additionally, the general population now trusts surgical intervention using metallic devices more than living with chronic pain, for example, in end-stage degenerative arthritis. Together, we are seeing a steadily increasing demand for biomaterials in a variety of devices. More than 5 out of every 100 persons above the age of 50 have knee implants in the US alone, and that number is greater than 2 out of every 100 people for hip implants. If dental implants and fracture fixation devices are included, more than 7 out of every 100 Americans of all ages have some kind of implant [2]. Yet, considering different metallic materials used for millions of people worldwide, there are only three primary metallic materials currently in use – (1) stainless steel (SS) 316L (primarily used in fracture management devices); (2) Commercially pure Titanium (CpTi) and Ti6Al4V (used in dental, spinal and orthopedic implants) and (3) CoCr alloy (used in articulating surfaces and some orthopedic weight-bearing applications). Other metals such as Ta, nitinol (NiTi), and magnesium alloys are also being used for non-load-bearing applications. Although these alloys have contributed to improving the quality of life for millions of people, further improvements are warranted to meet the growing demands, particularly from younger, more active patients or patients with compromised bone quality. For example, CoCr alloy, a wear-resistant material of choice, is typically used in femoral heads for total hip arthroplasty (THA) [1]. *In vivo* life of THAs is often reduced due to debris generation and Co and Cr metal ion release from taper junctions. On August 14, 2018, the European Federation of National Associations of Orthopedics and Traumatology (EFORT) under its new EU Medical Devices Regulation announced that medical devices that continue containing cobalt would need to indicate on the device or label that "cobalt, a purportedly 'cancer-causing' substance, is present" [2]. Similarly, SS316L containing 16–18% Cr has a very high elastic modulus (~193 GPa), which often leads to implant loosening due to a modulus mismatch with bone resulting in stress-shielding and bone fracture [3]. Over the past few decades, the orthopedic and the dental industry have focused on Ti and its alloys, primarily Ti6Al4V, for benefits stemming from good mechanical properties [3–6]. However, although mechanically more favorable for implant applications, Ti alloys have a relatively inherent bioinert surface. Numerous design alterations such as coatings of other metals like porous Ta, porous CpTi, or calcium phosphate ceramics have been implemented to improve Ti's biocompatibility [3,7–9]. Ta, on the other hand, is a relatively new biomedical implant material which has shown exceptional biocompatibility [4–7], but it

comes with several processing difficulties in the domain of implant fabrication. Inherent chemical properties of Ta such as high density (4 times > Ti), wear prone nature, and high melting point (~3200 K) make it difficult to manufacture Ta-based implants. Therefore, Ta's application has only been restricted to Ti implants' coatings to induce surface bioactivity, and porous titanium augments to replace lost cancellous bone areas. Surface modification treatments, even though successful, are segmental approaches that lack the feasibility to solve a systemic problem related to the material itself. In other words, while coating techniques provide a temporary solution, there remains the likelihood of coating failure at the material interface. Of note, these alloys were historically borrowed from aerospace and automotive industries for their excellent fatigue and corrosion resistance, as opposed to being designed specifically for their performance in the biomedical industry. Based on these examples, it is clear that there exists a need to innovate metallic alloys for biomedical applications such as in orthopedics and dentistry. The question we are posing here is - *can we design Ti-Ta alloy biomaterials incorporating the excellent biocompatibility of Ta and good mechanical properties and processability of Ti for biomedical applications?* In this research, we have evaluated Ti-Ta alloys' efficiency primarily from the standpoint of the biological response of the material bridging the length scale from macroscopic alloy design to microscopic porosity for tissue ingrowth to nanoscale porosity to enhance surface energy, Fig. 1a.

Various 3D Printing or additive manufacturing techniques make it relatively easy to design, innovate, and manufacture metallic parts with complex shapes on-demand. Apart from the relative ease of manufacturability in 3DP, patient specificity based on the application site's anatomy and "on-the-fly" design flexibility makes 3DP more useful for metallic implants. In comparison to conventional alloying routes for Ti-Ta systems such as high-temperature furnace melting followed by mold casting, 3DP aids to efficiently handle the large difference in melting temperatures of Ti and Ta. The use of focused high energy laser beams, control over melt pool characteristics, and minimizing *in situ* oxidation leads to efficient standalone part fabrication. Our work shows how the design and manufacturing flexibility of 3DP operations, notably the directed energy deposition (DED) technique, can help bring the exceptional biocompatibility of Ta together with excellent mechanical properties of Ti to innovate the next generation of metallic biomaterials for implants. Ideally, these materials should be suitable for both coatings as well as bulk structures. Since our work intends to develop technology using advanced materials translated into medical devices, we have used DED-based AM technology to add a porous coating on manufactured Ti6Al4V parts. Fig. 1b shows a schematic of how DED can add porous coating on an acetabular cup. We hypothesize that a novel bridging of multiple length scales in Ti-Ta alloys' composition and structure will enhance biocompatibility. Few studies have partially assessed alloys of Ti-Ta through mechanical characterizations and reported their superior mechanical properties over the individual components [10,11]. These alloys have reportedly shown excellent corrosion resistance and good mechanical compatibility with bone [12], presented in Table S1 in Supplementary document. However, these studies only established some of the mechanical properties of Ti-Ta alloys. There is still a knowledge gap regarding the biological response of Ti-Ta alloys, which is crucial in determining the efficacy of a device fabricated for the human body. We have processed Ti-Ta alloys combining CpTi with Ta using a DED based

Laser Engineered Net Shaping (LENS™). Our previous publication shows that LENS™ processing of pure Ti and pure Ta can be achieved under similar laser parameters [13]. The processing difficulties of conventional alloying can be avoided by employing DED of Ti-Ta alloys. Therefore, we wanted to use that knowledge to bridge length scales by macroscale addition of 10% and 25% Ta in CpTi, along with incorporating micro-porosities and nanoscale surface modifications to design materials for biomedical applications. We have evaluated the biological response using rat and rabbit distal femur implantation models. Surface modification through nanotube formation is considered a treatment on the base compositions (10Ta and 25Ta) and is abbreviated as 'NT' in the labels (CpTi-NT (TNT), 10Ta-NT and 25Ta-NT). Microporosity is considered the second treatment on the base compositions and is abbreviated as 'P' in the labels (CpTi-P, 10Ta-P, and 25Ta-P). Fig. 1 summarizes the overall objective of our research.

Methods

Sections below summarize preliminary information on materials and methods used in this study. Further details of methods have been described in the supplementary document.

Fabrication and processing of Ti and Ta implants using LENS™

Dense and porous Ti-Ta compositions were fabricated using the LENS™- 750 (Optomec Inc., Albuquerque, NM) system using pre-mixed powders of pure Ti and pure Ta, whereby 10%Ta and 25% Ta by weight were used on Ti6Al4V substrate. Ti6Al4V was used as a substrate material to evaluate interfacial microstructure for cracks and delamination while transitioning from Ti6Al4V alloy to CpTi-Ta alloy. The porous specimens had nonuniform residual porosities due to variation in processing parameters such as a more relaxed hatch distance and lower layer height. Following the fabrication, each composition's energy input density was carried out using Simchi's equation [44].

Material characterization

Cross-sectional microstructures of the interface between the 10Ta, 25Ta samples (12 mm diameter discs), and the Ti6Al4V substrate were examined using Field Emission Scanning Electron Microscopy (FESEM) imaging (FEI Quanta 200, FEI Inc., OR, USA). The contact angle measurements were done on 12 mm diameter discs through a sessile drop method using a face contact angle set up equipped with a microscope and a camera. A similar process was performed for surface energy calculation with polar and apolar liquids such as diiodomethane, ethylene glycol, and formamide. Surface energy was calculated using van Oss theory for metallic materials.

Vickers microhardness measurements were made with a Phase II Plus, Micro Vickers hardness tester (Upper Saddle River, NJ, USA) on the Ti-Ta compositions, interface and substrate regions using a 200 g load and dwelling time of 15 s on 12 mm diameter discs. Compression tests on as-fabricated porous Ti-Ta samples were performed using a screw-driven universal testing machine at an initial strain rate of 0.48 mm/min using cylindrical samples of 6 mm diameter and 10 mm long. Initial material characterization was followed by electrochemical anodization of the CpTi, 10Ta, and 25Ta rod type samples (6 mm

diameter and 10 mm long and 3 mm diameter and 5 mm long) to form nanotubes on the surface. Nanotubes surfaces were scratched to determine the dimensions of the nanotubes and were imaged using FESEM.

In vitro cellular attachment and cytocompatibility evaluation

TNT, 10Ta, 25Ta 12 mm diameter discs specimens were used for *in vitro* assessment (10 samples for each composition) with human fetal OB (hFOB) [American Type Culture Collection (ATCC), Manassas, VA] cells for 3 days to evaluate initial toxicity of the parent materials. Cell viability was characterized by MTT assay followed by FESEM imaging of cellular proliferation and attachment to the samples' surface.

In vivo study in rat distal femur

Male Sprague-Dawley rats with average weights between 280 and 300 g were used for the *in vivo* study. Surgeries were of the bilateral distal femur model by incorporation of a cylindrical defect. The bone defects were created using a drill bit at a distal epiphyseal location similar to the implant's dimensions (3 mm diameter × 5 mm long). The study was designed following an incomplete randomized block design. At a 5-week harvest, micro-CT analysis was performed to observe bone growth around the implant at the site of surgery. Biological evaluation of new bone formed was performed by cutting thin sections of resin-fixed bone blocks followed by Masson-Goldner's Trichrome staining to identify osseous tissues under a light microscope (Olympus BH-2, Olympus America Inc., USA) and SEM. Quantitative histomorphometric analysis was carried out using Gimp 2.8 software for a predetermined region of interest [45–49].

In vivo study in rabbit distal femur

Skeletally mature male New Zealand White rabbits with average weights between 3.5 and 4 kgs were used for the *in vivo* study. Bilateral cylindrical defects for implant placement were made in the distal femur. Implants (6 mm diameter × 10 mm long) were surgically placed unicortically through the distal epiphysis. The study was designed following an incomplete randomized block design for implant placements bilaterally. Three implants from each treatment group were randomly assigned to the left and right femurs of the rabbits ensuring statistically significant replication and randomization. At the study endpoint (7 weeks post-surgery), the harvested metal-bone explants were fixed in 10% neutral buffered formalin for at least 72 h for tissue infiltration. The bone-scaffold explants were dehydrated under a serial dehydration procedure for 25 days post-harvesting and fixed in methylmethacrylate (iMMA). The fixed bone blocks were cut into thick sections (~200 microns) using an Exakt band saw with a diamond blade from Exakt technologies (Oklahoma City, Oklahoma), followed by grinding/sanding to the desired thickness of 20–30 microns using Exakt 400 micro grinder with 1200 grit sanding paper.

The rabbit femoral explant sections were stained using Sanderson's Rapid Bone Staining (SRBS) [Sanderson's RBS + van Gie-son (S-CP3), Dorn and Hart, Microedge Inc., Loxley, AL] and Hematoxylin [Sigma Aldrich (H3136), St. Louis, MO] & Eosin [Surgipath, Leica, Buffalo Grove, IL] (H&E) staining for investigating osteoid, trabecular bone, blood vessels, and other tissue structures. Quantitative analysis of the implant-bone interface for the

biological response as a function of trabecular bone growth, blood vessel formation, bone remodeling, and bone apposition was conducted carefully by observing ten consecutive high magnification field optical images around the implant. Osseointegration at the bone-implant interface was examined as a function of the chemical composition of the apposing bone through energy dispersive X-ray [Octane Elect Energy Dispersive Spectroscopy (EDS) detector] and FESEM analysis [Apreo Volum-scope™]. All analyses were done based on an ROI of 250 micrometers as used previously for histological quantification.

Statistical analysis

All data are presented as the mean ± standard deviation and were analyzed using a one-way analysis of variance to test for significant comparisons. Post hoc Tukey-Kramer's test was used to determine the individual differences in means between treatments and control for multiple comparisons with a 95% confidence interval. Differences were considered significant at $P < 0.05$(*), $P < 0.001$(**). All statistical analyses were performed by JMP 14 (SAS Institute Inc., Cary, NC).

Results

Processing, physical, and mechanical properties of Ti-Ta alloys

The total energy input in any laser-based additive manufacturing is a direct measure of the process's feasibility. It is worth noting that the total energy input for 10Ta and 25Ta porous compositions is comparable to the total energy input for CpTi despite a large difference in melting temperatures and laser absorptivity of the two individual components. The relaxation in hatch distance allows for lesser melt pool overlap during processing coupled with lowering layer height, which de-focuses the laser, resulting in pores' formation. The average pore diameter was measured to be between 200 and 300 mm. All process parameters, along with the measured energy density, are shown in Table 1.

SEM micrograph in Fig. 2a reveals a phase transition at the cross-sectional interface. Ti6Al4V shows the characteristic microstructure of β-Ti while areas of α-Ti remain unresponsive to the etchant represented clearly by the lack of morphological details at the darker regions in the image [14]. In contrast to the typical Ti6Al4V microstructure, both the bulk and interface display martensitic α″ phase with a lamellar microstructure of Ta [10,15] due to the formation of rapidly quenched supersaturated bcc Ti-Ta solid solution [16]. This phase transition is mostly dependent on solute concentration and the quenching rate. In LENS™ operations, *in situ* quenching rates are very fast, typically between 10^3 and 10^5 K/s [17], combined with increasing addition of Ta from 10Ta to 25Ta results in microstructural variations. The presence of α-Ti from Ti6Al4V in addition to martensite α″ at the bulk/substrate interface causes lattice strains, which results in higher hardness than the substrate or the bulk regions. Similar lamellae formation is seen in both Ta compositions, but 25Ta shows more uniform and oriented platelet colonies due to higher Ta content. While 10Ta shows the formation of coarse arrays of lamellar platelets, 25Ta shows a refinement of platelets and more colonies with uniform orientation due to a decrease in the α″ phase and an increase in β-phase stability [10]. The 'interface' region shows very well fusion of CpTi-Ta alloy with the Ti6Al4V substrate, apparent from the lack of cracks or fusion defects,

showing similar lamellar microstructure in the sample region. Fig. 2b shows Ti and Ta elemental composition across the interface, respectively. Ta and aluminum (Al) were of particular interest to distinguish between the 10Ta and 25Ta compositions, and the Ti6Al4V substrate as Al is one of the inherent elements in Ti6Al4V. Quantitative analysis of 25Ta composition showed 18% Ta well mixed with Ti in addition to 6% Ta particles that did not melt. Similarly, 10Ta composition showed 6% Ta well mixed with Ti with 4% Ta particles present in the bulk material. Phase analysis of 10Ta and 25Ta compositions, Fig. 3a, corrobo-rates the formation of martensitic α″ phase as seen in Fig. 2a. Post compression test fractographic images, Fig. 2c, reveal fracture surfaces of CpTi, 10Ta, and 25Ta at a characteristic 45° angle to the longitudinal or loading axis along the slip plane while 100Ta showed a buckling type ductile deformation behavior that resisted cracking. Although the formation of these metastable phases affects material properties, which is an essential factor in biomedical device design, no specific findings could be concluded to understand the role of metastable phases on biological properties.

Hardness profiling across the interface between the alloyed samples and the substrate provides a clear understanding of alterations in material properties due to the addition of Ta in CpTi. Vickers diamond-indentation microhardness measurements for both 10Ta and 25Ta compositions exhibit a synergistic increase in hardness at the interface (Fig. 3b). This happened because of the solid solutioning between pure Ti and pure Ta [11]. Ti6Al4V substrate shows lower hardness (~310 ± 4 $HV_{0.2}$) than the interface (10Ta: 363 ± 7 $HV_{0.2}$ and 25Ta: 416 ± 3 $HV_{0.2}$) and the 10Ta and 25Ta bulk regions. Owing to the difference in melting point between CpTi (1953 K) and Ta (3273 K), the total laser energy input significantly varies during melt pool formation (CpTi: 4.9–5.5 J/mm^3, 25Ta: 7.2–7.9 J/mm^3), Table 1. At high temperatures, solid solution mixing occurs between pure Ti and pure Ta during laser heating followed by rapid quenching, whereby Ta solidifies much faster than Ti [8]. Upon further cooling, Ti solidifies at the grain boundaries of Ta, resulting in the formation of martensite α″ phase [10,15] and subsequently solid solution strengthening.

Compressive yield strength was 803 ± 70 MPa, 686 ± 13 MPa, 277 ± 2 MPa for 10Ta-P, 25Ta-P, and 100 Ta-P. A significant difference is observed from 10Ta-P to 25Ta-P based on the addition of Ta in Ti, which is following the hardness values of 10Ta and 25Ta compositions. The compressive behavior of the Ta alloys can be explained from the formation of α″ metastable martensitic phase. There are fewer slip systems present in the α″ crystal system as compared to a β-phase crystal structure, which results in higher stress requirement for plastic deformation of α″ than β phase matrix [18], which is noticed in 10Ta due to the formation of more coarse grains of α″ phase. However, increasing Ta addition results in a decrease in the alloys' compressive yield strength, indicating a reduction in brittle α″ and an increase in β-phase stability. Another important parameter when determining a metallic biomedical device's suitability is the elastic admissible strain, which is essentially the ratio between yield strength to the modulus. Our results suggest admissible strain for 10Ta~25Ta > CpTi, making Ta alloys mechanically more compatible for load-bearing applications. A decrease in the elastic modulus of CpTi with Ta's addition was also observed in Table 2, which is in accordance with findings in the literature [11]. The increase in interfacial hardness, refinement in microstructure, and low elastic modulus for both 10Ta and 25Ta compared to CpTi and Ti64 substrates indicate better mechanical biocompatibility

for their applications in biomedical devices both for coating and bulk applications. The lower modulus of a metallic implant is also beneficial for early-stage osseointegration.

Surface wettability and in vitro cell-material interaction

Surface wettability and *in vitro* cell-material interactions are important factors that determine the biocompatibility of a material. CpTi has already been established as a biocompatible material despite having moderate surface wettability; therefore, materials with close or similar surface wettability are deemed to have the same effect on cellular attachment and proliferation.

Our results for 10Ta and 25Ta suggest similar surface wettability (contact angles) to that of CpTi despite lower values of surface energy, Table 3. *In vitro* results for 10Ta and 25Ta show better osteoblast (OB) attachment and proliferation. We performed cytocompatibility tests on 10Ta and 25Ta to determine any possible toxicity exhibited by the base compositions compared to the titania nanotube (TNT) surface as a function of alloying with Ta. Since surface-modified CpTi has been proven to show enhanced cellular interaction [20,21], TNT was considered a control. Fig. 4a and 4b show well-flattened and attached OB cells on all the surfaces, including control at both 3 and 7 days of culture. After 7 days of culture, cells on 10Ta and 25Ta showed uniform spreading and filopodial and lamellipodial extensions. To support these findings, an MTT assay was performed to measure OB viability and cytotoxicity, Fig. 4c. Higher cell density was observed in 10Ta and 25Ta compositions compared to TNT. Thus, it can be said that 10Ta and 25Ta compositions are biocompatible and non-toxic on a static cellular level. It is important to note that 10Ta and 25Ta show no signs of cellular toxicity and enhanced cell-material interaction than TNT despite having lower surface energy than CpTi, meaning surface energy only plays a part towards a complete understanding of how cellular structures interact with the surface of a material.

Structural modifications and in vivo biological response

Cell-material interaction is only a part of the evaluation for efficiency in load-bearing applications. The biological performance of an implant through bone formation and osseointegration in dynamic *in vivo* conditions provides a complete picture of the implant material's efficacy in practical use. Therefore, it is crucial to study the biological interaction of the host osseous tissue with both surfaces and the bulk of the implant material. Studies have shown better *in vivo* tissue-material interaction for structurally modified implants compared to dense untreated implants. For example, nanotube modified Ti surfaces have shown better osseointegration compared to untreated Ti [20–22]. Nanoscale architectures are irregularities that are diametrically several orders larger in magnitude than molecular sizes (Fig. 5a (inset) 10Ta-NT: 88 ± 5 nm, 25Ta-NT: 67 ± 12 nm). Nanotubes provide enhanced surface area for interaction with the surrounding environment, which forms localized chemical, dipolar, or electro-static interactions with resident ions presented in physiological fluid [23,24], aiding in metallo-organic transitions. Besides, enhanced biological fixation has been reported for Ti implants with bulk microporosities [7,25], resulting in the better interlocking of material with host bone at the interface due to bone tissue infiltration. Based on *in vitro* cytotoxicity assessment, 10Ta and 25Ta compositions were augmented with surface modification to form nanotubes, Fig. 5a, as well as micro-porosities, were introduced

during fabrication of *in vivo* implants (Fig. 5b). The dense and porous specimens with and without nanotubes were investigated for a biological response using *in vivo* rat and rabbit distal femur models. Iatrogenic implants are desired to be in direct contact with bone to avoid any kind of aseptic loosening. Considering that *in vivo* surgery precision determines the implant's bone apposition, a correlation between size and shape of the implant and defect is essential, which is observed through computed tomography (CT) images and radiographs post-surgery, Fig. 5c, d.

In vivo biological response in a rat distal femur model

In this part of the study, CpTi, TNT, and TNT-P were considered control groups to have a clear understanding of the biological response as a function of osteoid or new bone formation from compositionally and structurally modified Ti-Ta alloys. Our goal here was to study the combined effect of Ta addition, porosity, and nanotube surface modification towards early-stage osseointegration. Histomorphometric quantification reveals enhanced osteoblast formation for both 10% and 25% Ta addition compared to control. 10Ta-NT, 10Ta-P, and 10Ta-P-NT compositions exhibit better performance than controls but are within the standard error of each other. These values can be correlated to qualitative histology micrographs, Fig. 6a, showing more implant-osseous tissue integrated regions for these compositions than control. However, 25Ta-NT, 25Ta-P, and 25Ta-P-NT compositions show significant differences in means from each other, with 25Ta-P-NT exhibiting a higher percentage osteoid surface per bone surface (OS/BS%) in contrast to 25Ta-NT and 25Ta-P as well as control, Fig. 6b. Histology also reveals better-integrated regions and fewer to no gaps at the tissue-material interface. Osseointegration at the bone-implant interface is a key factor in determining an implant's practical efficacy and longevity, meaning the more an implant is osseointegrated to the host bone, the faster the healing lowers the chances of physiological rejection. Except for CpTi and TNT, all other compositions show good bonding material with the host bone at the interface, Fig. 6c. It should be noted here that 10Ta-P-NT and 25Ta-P-NT demonstrate overlapping regions of bone tissue with the material surface to a point where a clear interface is not visible.

In vivo biological response in a rabbit distal femur model

To better understand Ta's effect towards *in vivo* biological response between 10%Ta and 25%Ta, the porous compositions were further evaluated for biological response in a rabbit distal femur *in vivo* model. In contrast to a rat model, the rabbit femur provides a larger bone area around the implant, which helps better understand biological response as a function of bone remodeling, neo-vasculature, and apposition, and bone maturation, i.e., trabecular bone formation. The study was performed for 7 weeks, and the explants were thereafter evaluated for histological outcomes with two different bone tissue staining. Fig. 7a and 7b reveal histological examination of the distal femurs from the iatrogenic material implantation rabbits with variable amounts of cortical and medullary bone proliferation around the implant. CpTi-P shows mildly dense bony proliferation of woven bone along the entire margin of the implant within the medulla and focal ingrowth of proliferative bone into the implant along the short axis in the medullary space. The presence of a thin band of proliferative fibrocartilage covers the outer edge of the implant contiguous with the cortical bone. 25Ta-P and 25Ta-P-NT exhibits moderately dense bony proliferation of woven bone at

the lateral cortex and along the entire long and short axis margins of the implant within the medullary canal. Bone marrow elements multifocally fill the medullary bone adjacent to the implant. The cortical bone of the lateral intercondylar fossa is segmentally thickened by proliferative bone. At the junction of the implant and the cortical bone, there is also a mild to moderate proliferation of the fibrocartilage that normally covers the cortical bone at this femur level for 10Ta-P. There is no evidence of inflammation, infection, neoplasia, or pathological fractures of the surrounding bone in any examined rabbit femurs. Interestingly, in 100Ta-P, the implant's proliferative bone grows multifocally into pores present in the implant material. Quantitative evaluation, Fig. 7c, of the bone-implant interface from ten consecutive high magnification optical fields show comparative % bone apposition for 25Ta-P-NT and 100Ta-P compositions. The percentage of trabecular bone and the total number of blood vessels is higher around the implant-bone interface for 25Ta-P-NT compared to CpTi-P as well as 100Ta-P. Other compositions vis-à-vis CpTi-P, 25Ta-P, 25Ta-P-NT, and 100Ta-P, revealed active bone remodeling fronts in 10 out of 10 optical fields, while 10Ta-P and 25Ta-P showed 2 out of 10 and 8 out of 10 remodeling fronts, respectively.

Quantification of in vivo osseointegration.

Osseointegration is an important factor that determines the physical bonding of the implant to the surrounding host bone as a function of osseous tissue apposition, interaction, and ingrowth into the implant. Osseointegration is defined as the direct attachment of implant material in apposition to bone without any intervening connective tissue. Qualitative evaluation of osseointegration is most commonly done by assessing the implant surface interface and host bone using SEM. While this is significant to understand the morphological features of the newly formed bone at the interface, it is also essential that the biochemical reactions occurring at the bone-implant interface be characterized. Therefore, a chemical basis for osseointegration is necessary to gain complete insight into the performance of the implant in terms of neo-osseous growth (Fig. 8(a–d) and Fig. 9(a–g)). The explant histological sections were used to perform energy dispersive X-ray (EDS) analysis in conjunction with SEM to evaluate the Ti-Ta alloy implants' qualitative and quantitative biological performance. Fig. 8(a–d) exhibits an elemental characterization of the osseous tissue at the bone-implant interface. Qualitatively, all four compositions show varying amounts of calcium (Ca) within the determined ROI and a consistent oxygen (O) presence in all the compositions. The presence of Ca indicates mineralized osseous tissue around the implants depending on the bioactivity of the material, while uniform O detection can be achieved from various sources such as bone itself, which is mostly made of calcium phosphates, the hemoglobin from blood vessels as well as self-passivated TiO_2 on the implant surface. However, only 25Ta-P-NT revealed a distinguishable phosphorous presence (P) over a larger area in the EDS mapping (Fig. 8c). Although P was detected in varying amounts in all compositions when analyzed over sections under high magnification, 25Ta-P-NT had a strong enough P detection signal even at low magnification. This can be mainly attributed to osteoid or new bone formation that still has active mineralization fronts consisting of phosphate ions, which are corroborated with the higher amount of O as shown in Fig. 9e.

Quantification of EDS spectra and live maps from elemental mapping reveals the amount of particular elements present around the implants and provides important information about elemental diffusion into the tissue directly in apposition with the implant. Fig. 9(a–g) exhibits areas of elemental diffusion for each composition. CpTi-P and 10Ta-P-NT show diffused Ti (Fig. 9a, b (green and yellow regions)) in the bony growth around the implants. The presence of majorly Ca/O rich areas indicates bone mineralization and small amounts of P, which can be attributed to osteoid linings evident from the histological analysis. In contrast, 25Ta-P-NT not only shows bone mineralization in the Ti diffused regions (Fig. 9c (green and yellow)) but also revealed a strong presence of P in the Ca/P/O region (red) indicative of continued osteoid formation and extended bone remodeling cycle. The observations in 25Ta-P-NT are similar in most aspects with that of 100Ta-P, validating our hypothesis that Ta alloyed with Ti in an amount as low as 25% can elicit similar biological performance as 100% Ta, thereby circumventing every processing and cost complexity associated with a pure Ta implant. However, a remarkable increase in Ca signature in the 25Ta-P-NT specimen reveals an accelerated bone maturation and calcification even compared to 100Ta-P, which indicates early-stage healing for 25Ta-P-NT compositions.

Discussion

Biological mechanism of Ti-Ta alloys in a physiological environment

Biological mechanisms of Ti-Ta alloys depend on a convergence of chemical and structural properties, which lead to enhanced biochemical reactions occurring at the surface of the implants. These functions can range from protein and other biomolecule adsorption on the implants' surface [26,27] to tissue integration through micropores in bulk [28,29] and overall structural stabilization of the device at the surgical site. This leads to accelerated tissue-material interactions through the upregulation of genetic markers uniquely responsible for osteogenesis. The two primary factors responsible for Ti-Ta alloys' enhanced biological performance are (1) anodic formation of co-existing surface oxide layers of TiO_2 and Ta_2O_5 and (2) nano-architecture of the oxide layers leading to higher surface area for biochemical reactions to take place. From literature, XRD investigation, and anodic polarization measurements of Ti-Ta alloys have shown higher tendencies of Ta_2O_5 formation on the surface of these implants with an increase in Ta content [12]. XRD analysis revealed predominant Ta_2O_5 peaks for Ti-30%Ta as compared to TiO_2 signature peaks for Ti-10%Ta compositions. The presence of higher Ta oxide with an increase in Ta content can be attributed to the higher negative free energy of formation for Ta_2O_5, which leads to higher stability of the oxide layer evident from noble shift in anodic polarization curves. Besides, pristine points of zero charge (PPZC) for Ti and Ta oxides have been evaluated to lie below pH6 [30]. Surface charge density and zeta potential of such sparingly soluble oxides are negative at pH values above PPZC. Surface charge is an important factor in determining ions' driving forces interacting with such oxide layers in a physiological environment. For example, Ti and Ta oxides would acquire an overall negative charge in simulated body fluid (SBF), which leads to a cascade of biochemical reactions occurring at the surface, as reported in the literature. Therefore, for the compositions used in this study, it can be deduced that anodized 10Ta-NT and 25Ta-NT have predominant TiO_2 and Ta_2O_5 surface oxide layers, and the formation of structured nanotubes within these oxide layers aid in the

higher surface area leading to higher surface charge density [31]. This assumption was further clarified using elemental analysis of thin sections of tissue-material interfaces (Fig. 10a), where the 25Ta-NT interface showed a clear presence of diffused Ta and O into the adjacent bone tissue area. These two phenomena occurring in tandem result in biological enhancement of tissue interaction of these 3D printed implants. Fig. 10b represents a schematic of Ti-Ta surfaces' biological mechanism in promoting cell-material interactions based on literature evidence. A detailed description of the process of surface chemistry and architecture influencing initial cascades of protein adsorption, thereby initiating tissue integration, has been provided in the Supplementary information [32–36].

Bridging the length scales in biomedical device design

A vast majority of the biochemical and biomechanical functions occurring at the implant-host tissue interface immediately after surgical implantation of a biomedical device pan over multiple length scales. These multiscale processes stem from the inherent hierarchical heterogeneous bone structure [37] via continuous remodeling of natural bone where structures such as osteoids undergo substantial remodeling while interstitial/trabecular bone exhibits a higher degree of mineralization [38]. Achieving such hierarchical functionality on a material level for biomedical devices has been researched for the past few decades with bone mimicking ceramic scaffolds and polymer grafts [27,34]. However, achieving a similar hierarchical design in metallic devices was still a farfetched idea due to various processing difficulties associated with metal fabrication, specifically through conventional routes. Over the past four decades, the common approach towards enhancing the biological response of metallic devices has been either coating calcium phosphates [35,36] and other porous metals or biologics such as synthetic osteogenic drugs, growth factors, collagen, and hyaluronic acid [26,27,36,42]. However, the researchers and the industry failed to identify these modifications' adverse effects, such as coating failure, implant loosening, ectopic bone formation, inflammation, and tumorigenesis [43]. Considering such shortcomings, the question remained if there was a way to design new alloys specifically for biomedical devices that can overcome the hindrances and lead to faster healing. Alloy material with a multifaceted structural design that can represent the natural coexisting multiple length scales in bone surely can have the potential to overcome those hindrances. Finally, since Ta is ~20 times more expensive than Ti, having a melting point ~2 times that of Ti, and density nearly 4 times that of Ti, innovation in Ti-Ta alloys, having similar biological response as pure Ta, will be ideal for the next generation of metallic implants that will be cheaper to manufacture with improved durability, and can be used in coatings or bulk structures.

Conclusions

Returning to first principles to identify the problem at a material level helped us design multiscale structural metal implants using 3DP, leading to the parent alloy's enhanced biological response (Ti-Ta) and mitigate problems associated with current practices. Bridging length scales on a hierarchical level to include hetero-geneity in structure can often result in complications and poor mechanical properties in implants that were successfully overcome in this study. Our results show a synergized enhancement of both mechanical and biological properties in the Ti-Ta implants. To elaborate, alloying Ta with Ti during additive

fabrication resulted in an overall decrease in Ti's elastic modulus (Ti: 110 GPa, 25Ta: 64 ± 6 GPa), which can help circumvent any mechanical instability that can arise from a very high mismatch in modulus. Extensive studies have been undertaken to explore porous materials in bone growth, starting from enhanced tissue regeneration to increased oxygen diffusion and cell migration. Consequently, porous Ti-Ta alloys exhibited increased osseous tissue formation at the implant-bone interface (70% trabecular bone formation in rabbit femur), providing evidence of the superior biological performance of the material towards early-stage bone healing. Osteocytic processes dimensionally range in the nanometer length scales; therefore, nanoscale design elements at the surface of an implant can also be expected to enhance migration of cells, adhesion, and influence overall bone remodeling (80% trabecular bone formation and 10/10 remodeling fronts in rabbit femur). Our results for 10Ta-NT and 25Ta-NT suggest a similar *in vivo* biological response compared to 100Ta, which sub-stantiates our initial hypothesis of Ti-Ta alloy with a low Ta content that can perform similarly as pure Ta. 3D Printing of Ti-Ta alloys allowed us to design next-generation biomedical alloys and structures by bridging hierarchical length scales and achieving superior biological performance through the enhanced early-stage bone formation reduced healing time. The Ti-Ta alloy implants offer a longer-term solution for structurally suitable orthopedic or dental devices and serve as an excellent template for designing the next generation of biomaterials in the future.

Supplementary Material

Refer to Web version on PubMed Central for supplementary material.

Acknowledgements

The research reported in this publication was supported by the National Institute of Arthritis and Musculoskeletal and Skin Diseases of the National Institutes of Health under Award Number R01 AR067306-01. The content is solely the authors' responsibility and does not necessarily represent the official views of the National Institutes of Health. I.M and A.B would also like to acknowledge Yanning Zhang for his help in drafting the schematics.

References

[1]. Cooper HJ, J. Arthroplasty 31 (2016) 1381–1384. [PubMed: 27113943]
[2]. MedTech Eur. (n.d.).
[3]. Heinl P et al., Acta Biomater. 4 (2008) 1536–1544. [PubMed: 18467197]
[4]. Li X et al., Rapid Prototyp. J 16 (2010) 44–49.
[5]. Zhang S et al., Mater. Des 63 (2014) 185–193.
[6]. Bose S et al., Prog. Mater. Sci 93 (2018) 45–111. [PubMed: 31406390]
[7]. Bandyopadhyay A et al., Acta Biomater. 6 (2010) 1640–1648. [PubMed: 19913643]
[8]. Balla VK et al., Acta Biomater. 6 (2010) 2329–2334. [PubMed: 19931654]
[9]. Krishna BV et al., Acta Biomater. 4 (2008) 697–706. [PubMed: 18054298]
[10]. Zhou YL, Niinomi M, Akahori T, Mater. Sci. Eng. A 371 (2004) 283–290.
[11]. Zhou Y-L, Niinomi M, Mater. Sci. Eng. C 29 (2009) 1061–1065.
[12]. Zhou YL et al., Mater. Sci. Eng. A 398 (2005) 28–36.
[13]. Bandyopadhyay A et al., Addit. Manuf 28 (2019) 259–266. [PubMed: 31406683]
[14]. Gammon LM et al., ASM Handb. 9 (2004) 899–917.
[15]. Sing SL, Yeong WY, Wiria FE, J. Alloys Compd 660 (2016) 461–470.
[16]. Murray JL, Bull. Alloy Phase Diagr 2 (1981) 62–66.

[17]. Sahasrabudhe H, Soderlind J, Bandyopadhyay A, J. Mech. Behav. Biomed. Mater 53 (2016) 239–249. [PubMed: 26344856]

[18]. Ren Y et al., Mater. Sci. Eng. A 562 (2013) 137–143.

[19]. Bywater KA, Christian JW, Philos. Mag 25 (1972) 1249–1273.

[20]. Das K, Bose S, Bandyopadhyay A, J. Biomed. Mater. Res. A 90 (2009) 225–237. [PubMed: 18496867]

[21]. Das K, Bandyopadhyay A, Bose S, J. Am. Ceram. Soc 91 (2008) 2808–2814.

[22]. Bose S, Bandyopadhyay A, Modified Metal Materials, Surface Modifications to Improve Cell Interactions and Antimicrobial Properties, and Methods for Modifying Metal Surface Properties, (2013) U.S. Patent # 8,545,559.

[23]. Albrektsson T et al., Ann. Biomed. Eng 11 (1983) 1–27.

[24]. Sundgren JE, Bodö P, Lundström I, J. Colloid Interface Sci 110 (1986) 9–20.

[25]. Balla VK et al., Acta Biomater. 6 (2010) 3349–3359. [PubMed: 20132912]

[26]. Place ES, Evans ND, Stevens MM, Nat. Mater 8 (2009) 457–470. [PubMed: 19458646]

[27]. Ducheyne P, Mauck RL, Smith DH, Nat. Mater 11 (2012) 652–654. [PubMed: 22825010]

[28]. Bobyn JD et al., J Bone Jt. Surg Br 81 (1999) 907–914.

[29]. Hollister SJ, Nat. Mater 4 (2005) 518–524. [PubMed: 16003400]

[30]. Kosmulski M, Langmuir 13 (1997) 6315–6320.

[31]. Miyazaki T et al., Biomaterials 23 (2002) 827–832. [PubMed: 11771702]

[32]. Xu J et al., J. Mater. Chem. B 3 (2015) 4082. [PubMed: 32262630]

[33]. Mihranyan A et al., Langmuir 25 (2009) 1292–1295. [PubMed: 19115807]

[34]. Li P et al., J. Biomed. Mater. Res. A 28 (1994) 7–15.

[35]. Wang N et al., A.C.S. Appl Mater. Interfaces 4 (2012) 4516–4523.

[36]. Capellato P et al., Engineering 05 (2013) 707–713.

[37]. Lakes R, Nature 361 (1993) 511–515.

[38]. Rho J-Y, Kuhn-Spearing L, Zioupos P, Med. Eng. Phys 20 (1998) 92–102. [PubMed: 9679227]

[39]. Wegst UGK et al., Nat. Mater 14 (2015) 23–36. [PubMed: 25344782]

[40]. Li X et al., Sci. Adv 5 (2019) eaay6484. [PubMed: 31763458]

[41]. Shah NJ et al., Sci. Transl. Med 5 (2013). 191ra83–191ra83.

[42]. Wagner DO, et al., Sci. Signal 3 (2010) mr1–mr1 [PubMed: 20124549]

[43]. James AW et al., Tissue Eng. Part B Rev 22 (2016) 284–297. [PubMed: 26857241]

[44]. Simchi A, Pohl H, Mater. Sci. Eng. A 383 (2004) 191–200.

[45]. Parfitt AM et al., J. Bone Miner. Res 2 (1987) 595–610. [PubMed: 3455637]

[46]. He T et al., Sci. Rep 7 (2017) 16270. [PubMed: 29176604]

[47]. Vandeweghe S et al., J. Biomed. Mater. Res. B Appl. Biomater 101 (2013) 1259–1266. [PubMed: 23661363]

[48]. Li K et al., Sci. Rep 8 (2018) 1843. [PubMed: 29382859]

[49]. Bandyopadhyay A et al., Acta Biomater. 96 (2019) 686–693. [PubMed: 31326668]

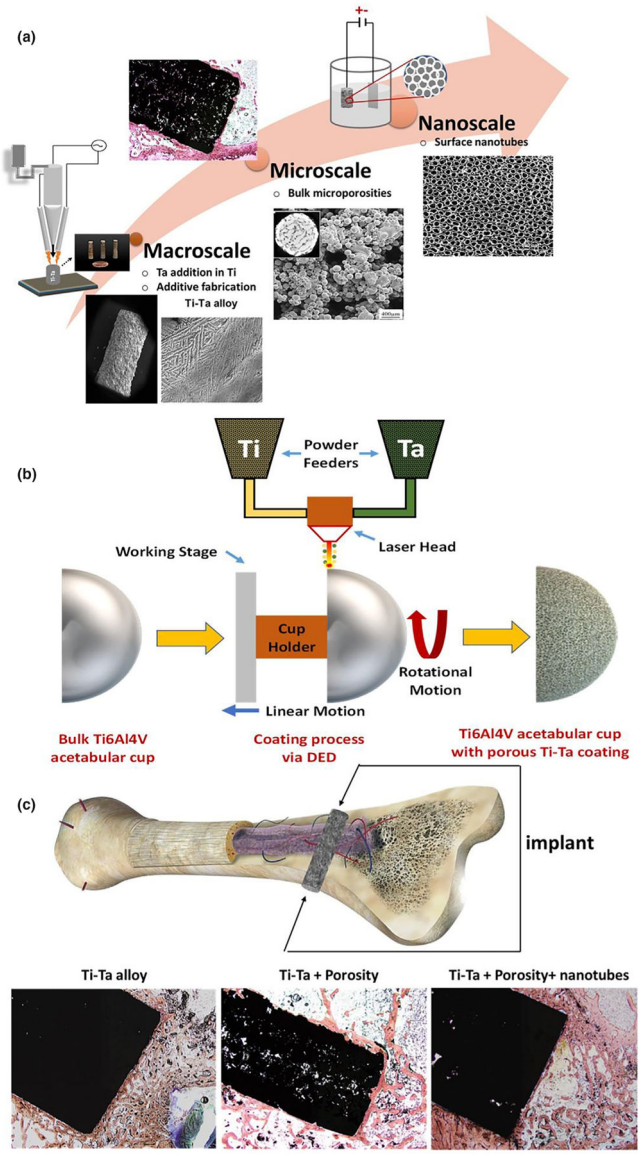

FIGURE 1.

Designing Ti-Ta alloys via 3D Printing. a. Additive fabrication of Ti-Ta alloys through bridging length scales by macroscale addition of Ta in Ti, incorporating microporosities during processing and *in situ* nanoscale surface modification. b. Schematic of directed energy deposition (DED) process for Ti-Ta alloys coating on a prefabricated acetabular cup. c. Cross-section of human bone exhibiting multiscale osseous structures starting from the macro transition from cortical to cancellous bone, microporous network structures in the cancellous bone, and nanoscale collagen filaments called osteons [http://www.buharainsaat.net/view/100305/accessed11.16.19]. Biological performance evaluation of designed Ti-Ta implants based on variations in composition, microporosities, and nanotube surface modifications.

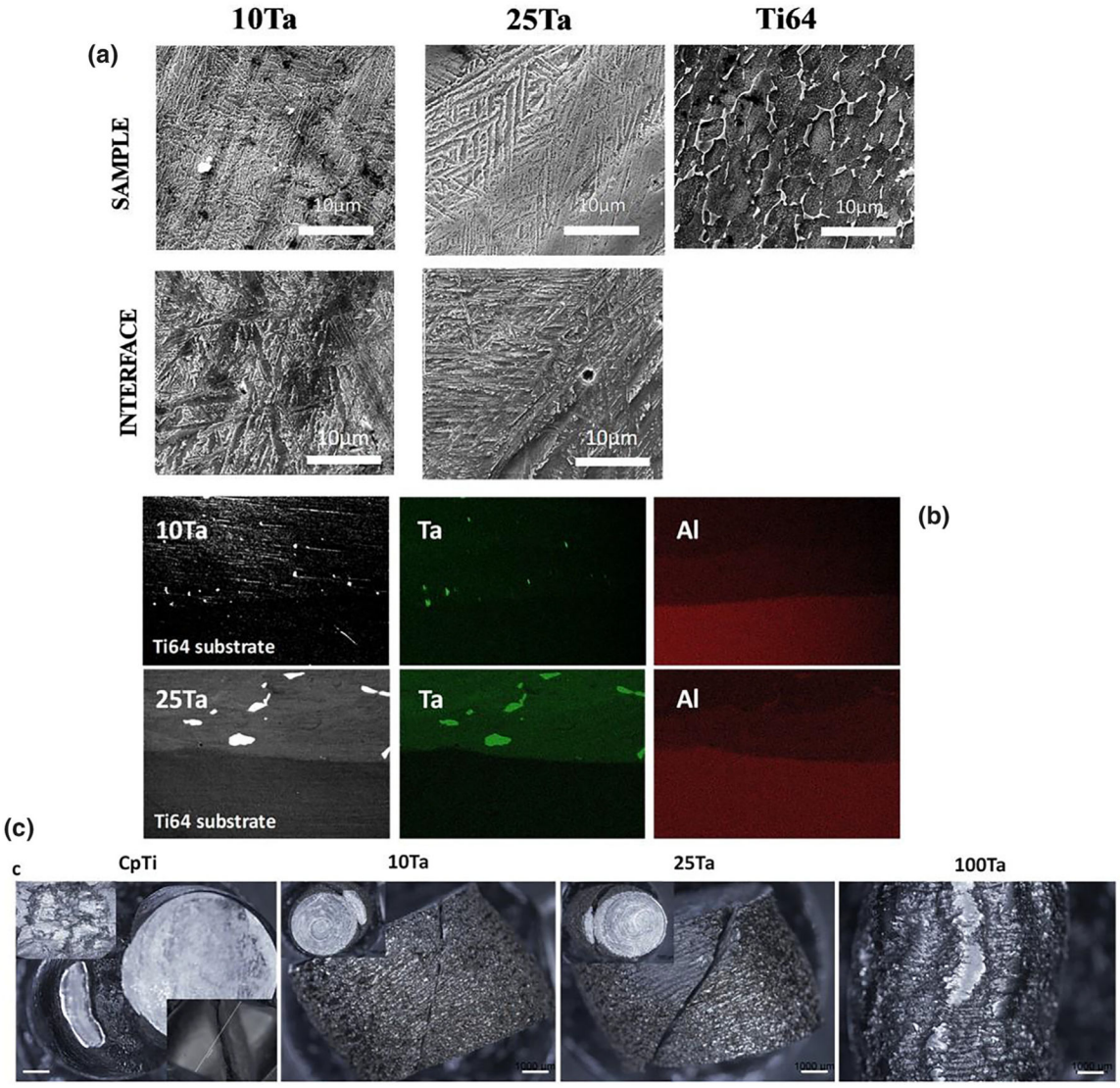

FIGURE 2.

From concept to material testing, a. SEM micrograph showing microstructures of the substrate, interface, and the alloyed regions of the 3D Printed compositions. Both 10Ta and 25Ta show characteristic martensite lamellae at the alloy as well as interface regions. The microstructural morphologies of Ti-Ta alloy change with increasing Ta content. 10Ta shows the formation of coarse arrays of lamellar platelets, whereas 25Ta shows finer platelets and more colonies with uniform orientation. The microstructure of the sample and interface region shows contrasting differences from that of the Ti6Al4V substrate due to the presence of Ta. b. Elemental mapping of 10Ta and 25Ta reveals the presence of Ta in the sample regions in contrast to Ti6Al4V substrate. Aluminum is found in the substrate, which is observed to have diffused in the first laser pass zone into the sample, c. Micrographs of fracture surfaces of porous samples showing crack propagation along slip plane for CpTi-P, 10Ta-P, and 25Ta-P and ductile deformation for 100Ta-P. Scale bars in 2c represent 1000 μm.

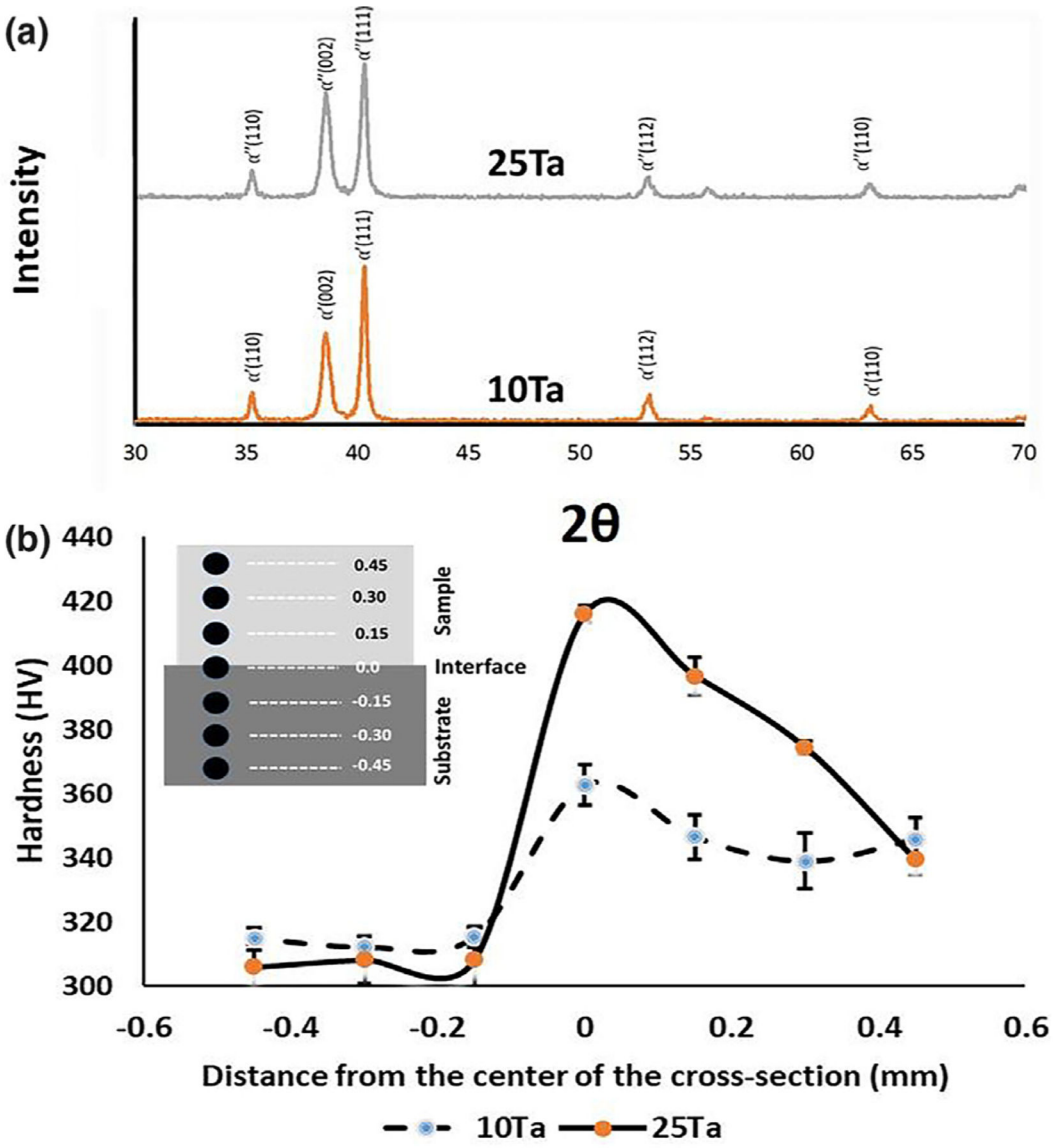

FIGURE 3.

a. Phase analysis using X-ray diffraction. XRD peaks for Ti-10Ta and Ti-25Ta show martensitic α′ and α″ metastable phases, respectively, due to the rapid quenching of Ti-Ta solid solution giving rise to metastable phases [19], b. variation of hardness across the sample-substrate interface for 10Ta and 25Ta. Inset shows a schematic drawing of the experimental method. Hardness for the 10Ta sample and interface regions were 344 ± 3 $HV_{0.2}$ and 363 ± 6 $HV_{0.2}$, respectively, which is higher than the hardness of Ti6Al4V 314 ± 1 $HV_{0.2}$. A similar trend was seen in 25Ta composition with increased hardness at interface region 416 ± 3 $HV_{0.2}$ as compared to the average hardness of substrate 308 ± 1 $HV_{0.2}$. Statistical analyses were done using one-way-ANOVA.

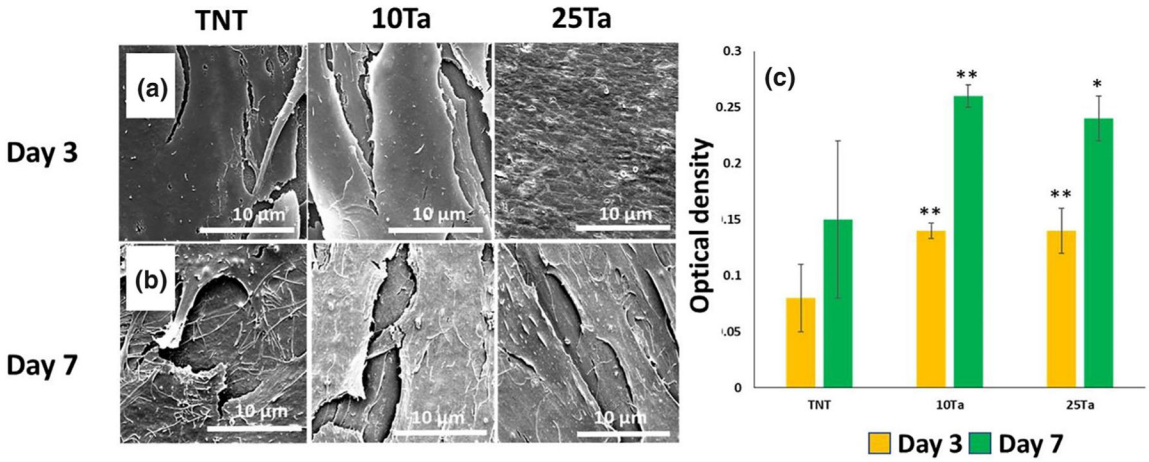

FIGURE 4.

Evaluation of *in vitro* cell-material interaction. a, b. Field Emission Scanning Electron Microscopy (FESEM) micrographs of OB cultured on control and base compositions for 3 and 7 days, respectively. Images show well-flattened cells with filopodial extensions and uniform substrate area coverage. A more uniformly flattened and layered OB cellular morphology was observed in SEM micrographs for 25Ta composition, c. shows MTT analysis of cytotoxicity in 10Ta and 25Ta compositions at 3 and 7 days. Cell viability increases in the presence of Ta, evident from MTT assay for 3 and 7 days. SEM observations for Fig. 4a,b. were done on multiple samples for each composition ($n = 3$) for uniformity. A sample size of $n = 3$ for each composition was considered for MTT analysis, with a triplicate observation made for each sample. The bar chart in Fig. 4c represents mean values for optical density. Statistical analyses were done using one-way ANOVA corrected for multiple comparisons with Dunnett's test for compositions compared to TNT control. ** – extremely significant difference and * – a significant difference.

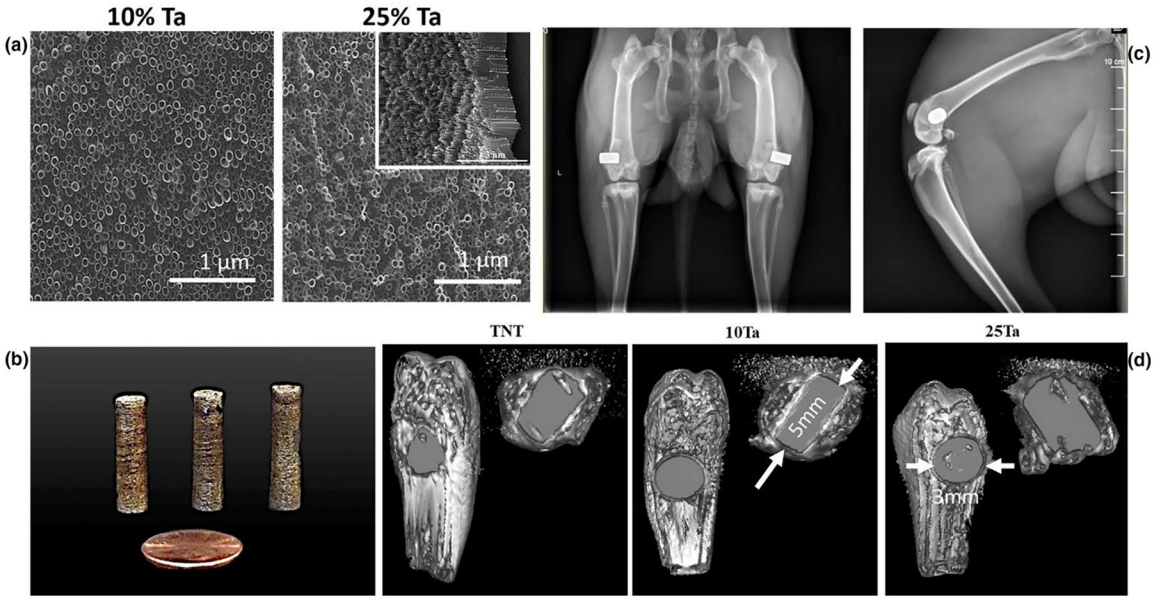

FIGURE 5.

Evaluation of implant surface and *in vivo* surgical apposition, a. SEM micrographs of nanotube surface-modified 10Ta and 25Ta compositions showing uniform growth of nanotubes in both. The nanotubes' length and diameter on the surface were calculated through a scratch test and SEM imaging. The average inner diameter and length of the nanotubes formed on the 10Ta-NT were 88 ± 5 nm and 1 mm, respectively; whereas the average inner diameter and length of the nanotubes formed on 25Ta-NT were 67 ± 12 nm and 1 μm, respectively. b. shows images of the 10Ta-NT and 25Ta-NT as processed samples, c, d shows the radiograph and CT scan images, respectively, of the bone-implant conjugate for TNT and Ta alloys. Proper placement of the implants was observed in 5-week harvested rat femurs and 7-weeks post-operative rabbit femurs (radiograph). CT images of the distal femur implant site within the femur confirm the close apposition of the metallic implant with bone tissue and dimensional correlation of the implant with the surgically created critical defect. Arrows indicate the dimensions of the implants. All tomographs were taken at an equivalent layer number from the sagittal plane.

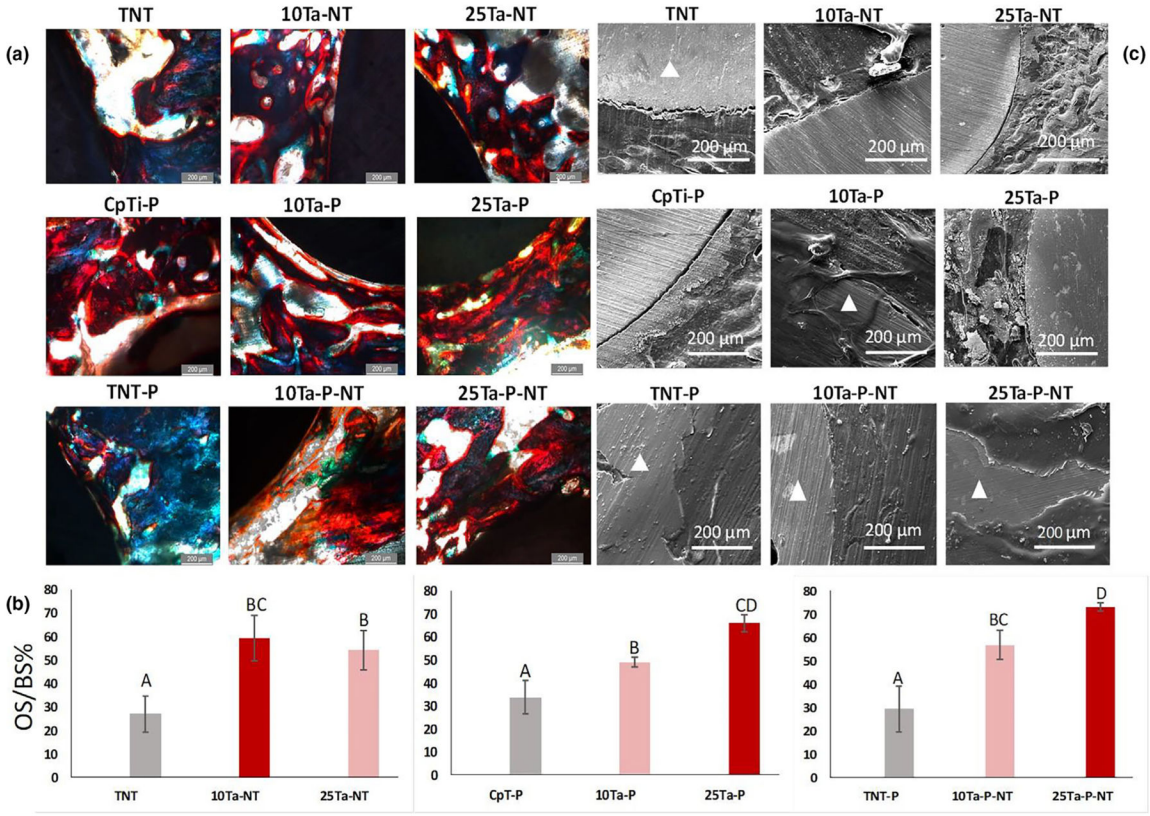

FIGURE 6.

a. Histological evaluation on the 300 μm thin sections of the Spurr embedded explant femurs reveals early-stage osteoid formation in both the 10Ta-NT and 25Ta-NT at 5-weeks. Osteoid presence was marked via red color from Modified Masson Goldner's stain. Nonuniform osteoid formation along the bone-implant interface was observed for the TNT (control). In comparison to TNT, 10Ta-NT and 25Ta-NT show a higher presence of osteoid, measuring 59 ± 10% and 54 ± 8%, respectively. Scale bars measure 200 μm. b. graphs represent quantitative histomorphometric representation of the OS/BS% in histology micrographs. All compositions show higher osteoid formation compared to control (CpTi-P, TNT, TNT-P). A sample size of $n = 6$ was considered for each composition, and statistical analysis was done on the histomorphometric data using one-way ANOVA with Tukey–Kramer correction for the pairwise comparison for means. Mean observations with standard deviation have been reported in the bar charts. Means that do not share a letter are significantly different, c. SEM micrographs of the bone-implant interface reveal the presence of noticeable gaps in TNT, indicating limited osseointegration. The 25Ta-NT displays decreased gap width compared to TNT. However, 10Ta-NT shows very well integrated osseous tissue at the bone-implant interface at 5 weeks post-implantation. Triangle shapes mark the implant area in the micrographs.

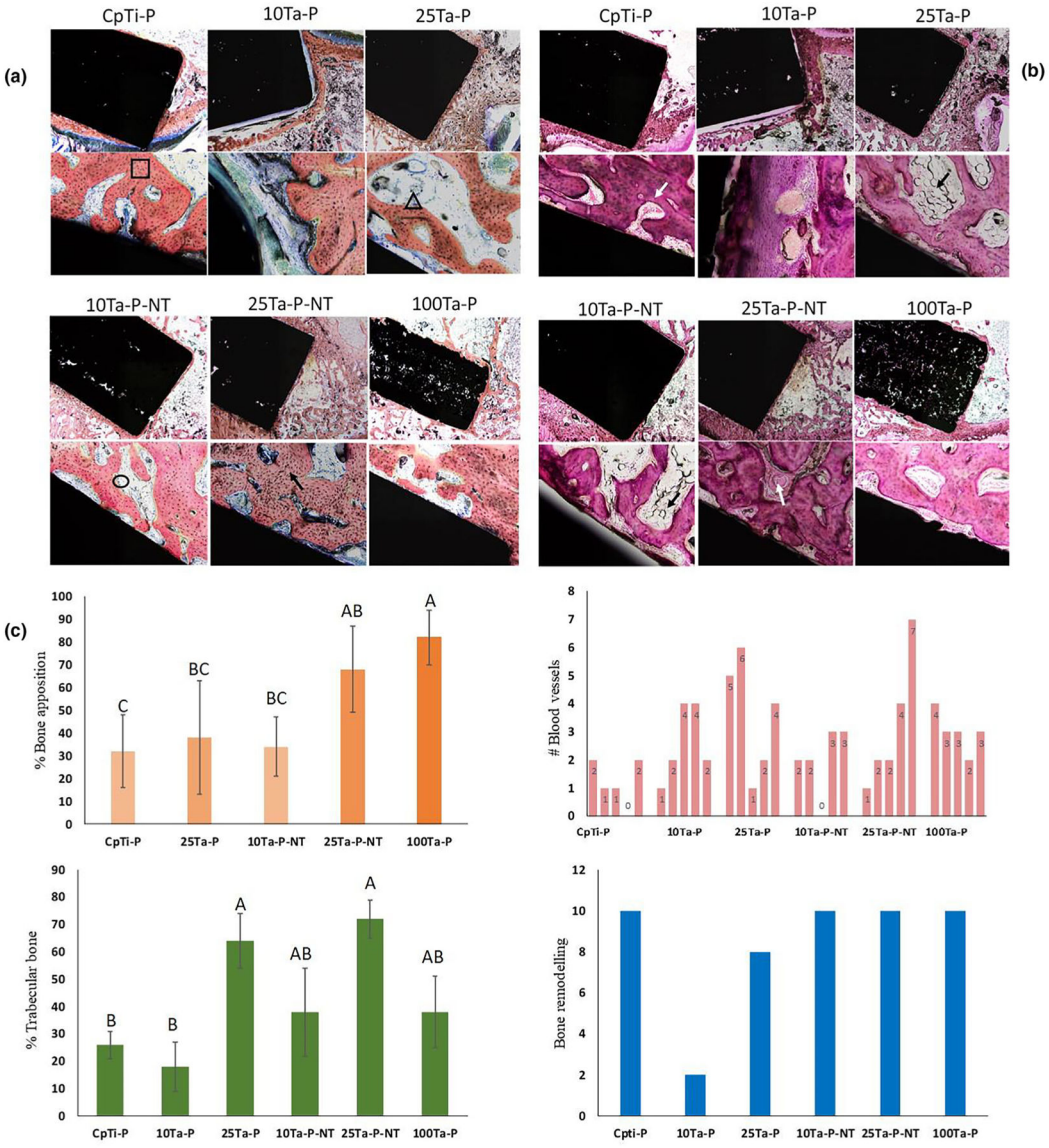

FIGURE 7.

a. Histology micrographs of tissue cross-sections stained with Sanderson's Rapid Bone Staining (SRBS) showing implant area in black, trabecular bone in light orange, and osteoid lining in blueish gray. 25Ta-P and 25Ta-P-NT samples show higher trabecular bone formation compared to the others. 10Ta-P-NT shows osteoid lining along the active mineralization front of the trabecular bone (black circle). Black square and triangle shapes show osteoblasts embedded in the trabecular bone and osteoclast activity at the lining of trabecular bone, b. micrographs show tissue cross-sections stained with Hematoxylin and Eosin (H&E) staining to reveal the presence of blood vessels (white arrow), inflammatory response, and adipose tissue embedding in the extracellular matrix (black arrow). No inflammatory response was noticed. The scale of images for a and b has been presented in the calculation of the methods section, c. quantitative plots of biological response evaluated from histology micrographs. 25Ta-P-NT shows higher trabecular bone formation as well as

the presence of blood vessels. Bone remodeling is active in all compositions except 10Ta-P. A sample size of $n = 3$ was considered for each composition, and statistical analysis was done on the histomorphometric data using one-way ANOVA with Tukey-Kramer correction for the pairwise comparison for means. The mean observations have been reported in plots for %bone apposition and % trabecular bone. Means that do not share a letter are significantly different. The bar graph for #blood vessels represents the total number of blood vessels counted in 10 consecutive high magnification fields around the implant. The bar graph for bone remodeling represents the number of active bone-remodeling fronts for each composition observed over 10 consecutive high magnification fields.

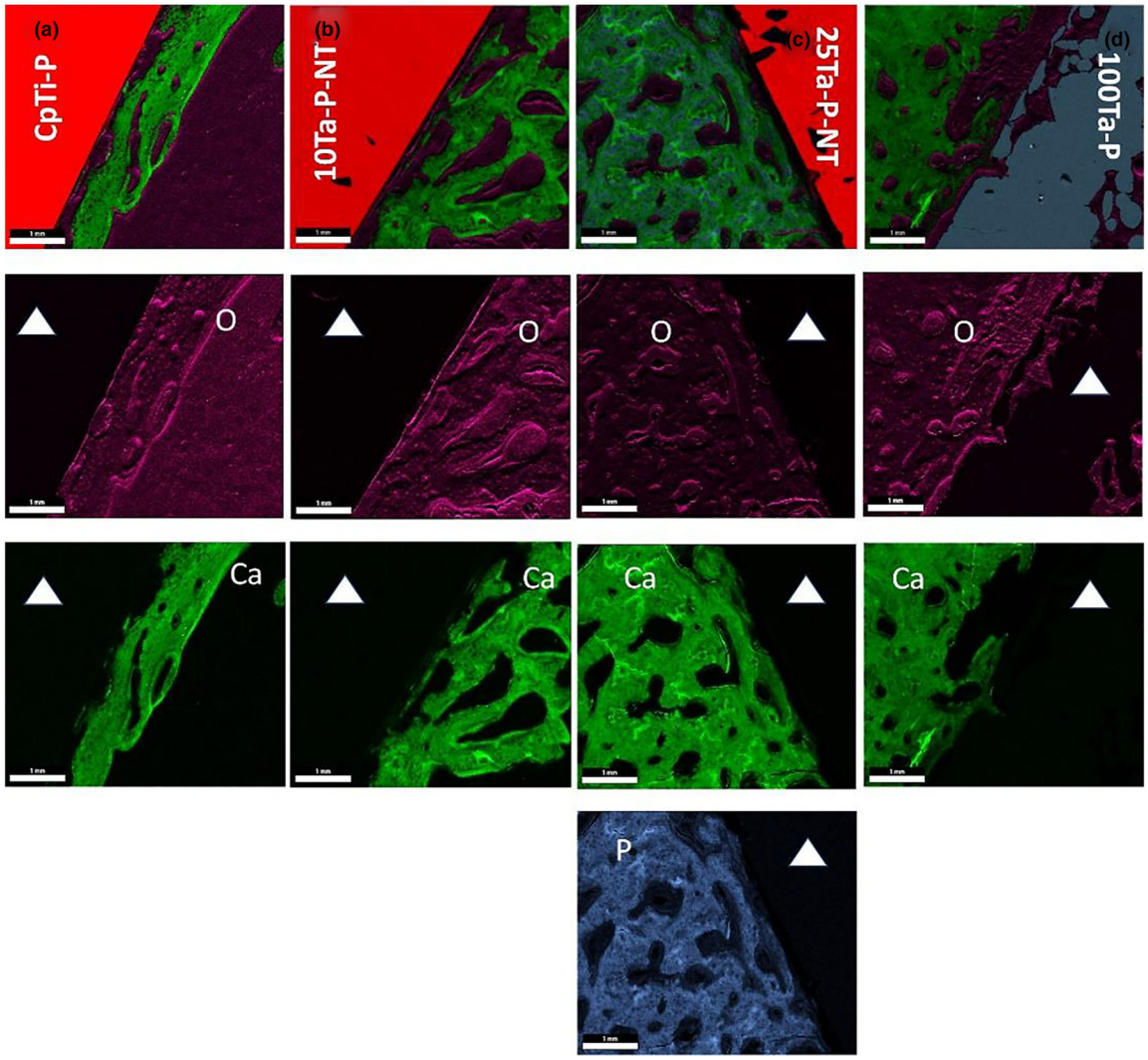

FIGURE 8.

EDS overlay mapping for CpTi-P (a), 10Ta-P-NT (b), 25Ta-P-NT (c), and 100Ta-P (d) rabbit histology sections showing regions of dominant oxygen, calcium, and phosphorous presence at the bone-implant interface. The presence of calcium is detected in all compositions in varying amounts depending on the implant material, whereas oxygen is seen to be uniformly present likely because bone and other biological structures such as collagen, extracellular matrix, and hemoglobin contain oxygen. A strong presence of phosphorous is observed in 25Ta-P-NT indicative of continued osteoid formation. The white solid triangle represents the implant region. Scale bars measure 1000 μm.

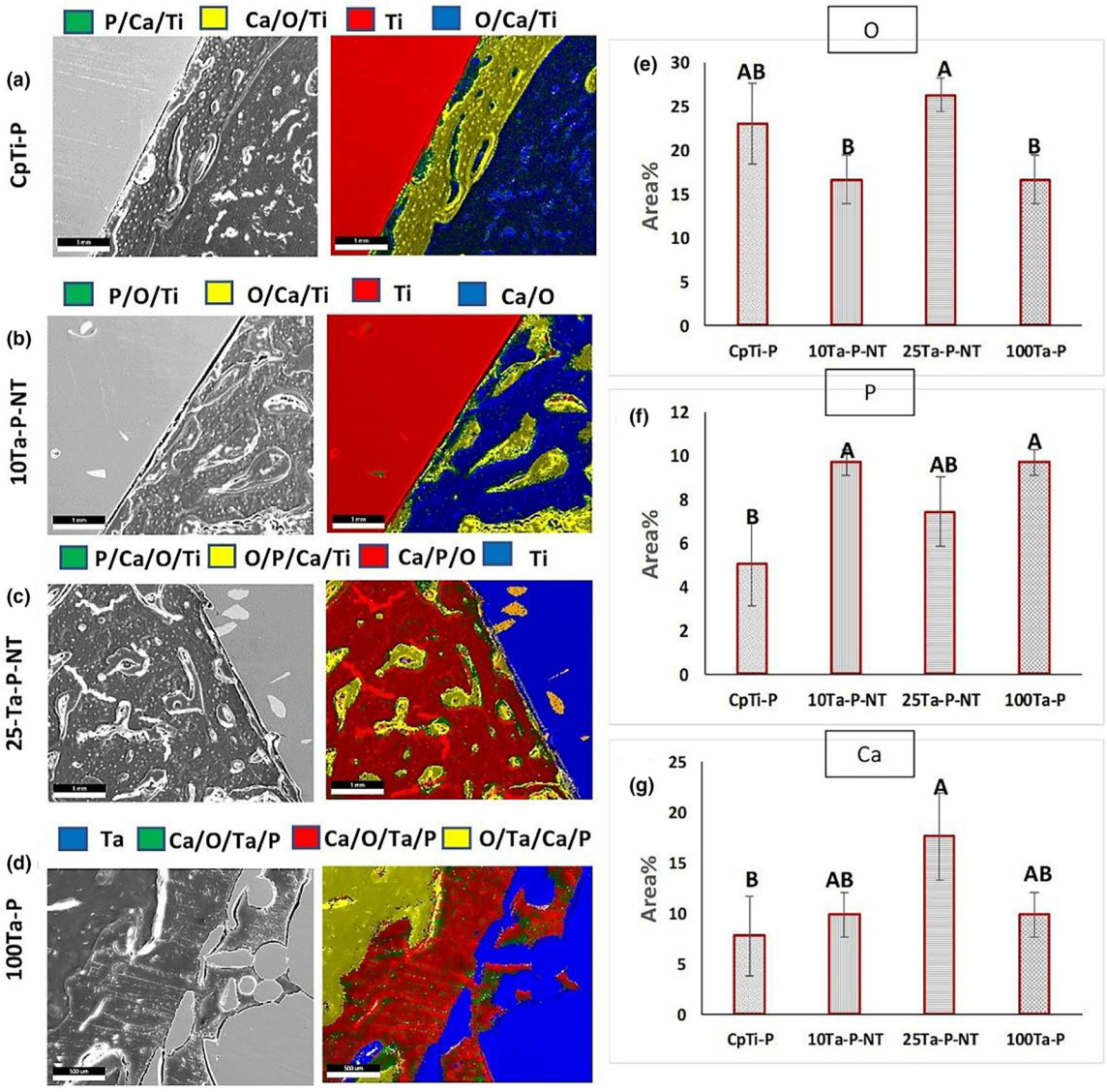

FIGURE 9.

(a–d) EDS live mapping for elemental detection showing different zonal diffusion of detectable elements. The left column represents SEM micrographs of the examined area, and the right column represents EDS live maps. (e–g) exhibits quantification of major elements detected during the live mapping around the implants (O, P, and Ca). The same sample size of $n = 3$ was considered for each composition, and statistical analysis was done on the EDS data using one-way ANOVA with Tukey–Kramer correction for the pairwise comparison for means. Means that do not share a letter are statistically significantly different. Scale bars measure 1mm or 1000 microns.

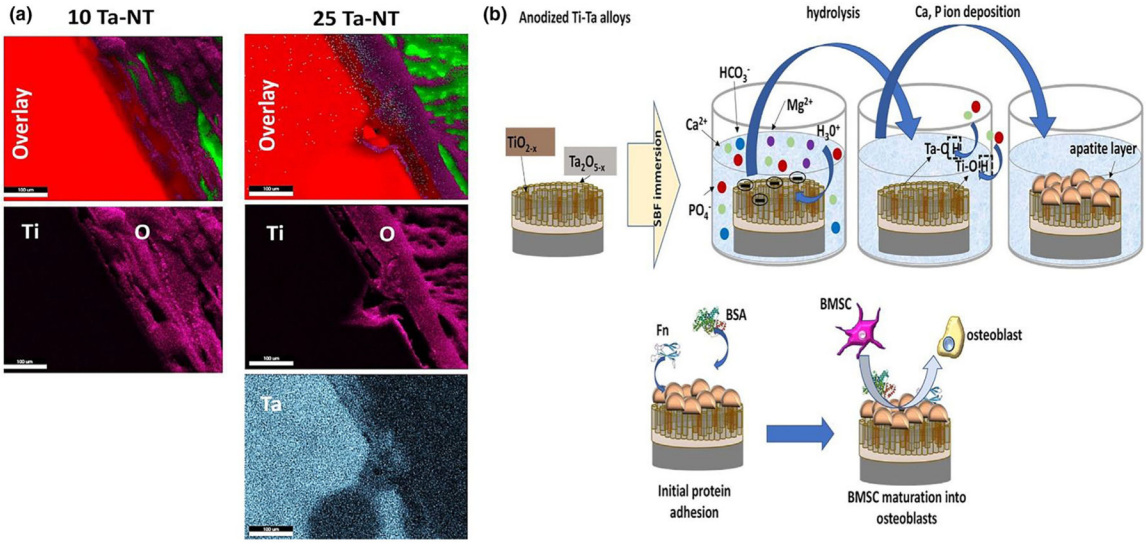

FIGURE 10.

a. EDS mapping of the tissue-material interface of the *in vivo* histological sections for 10Ta-NT and 25Ta-NT specimens showing signatures of detectable elemental Ta in the 25Ta-NT as opposed to in 10Ta-NT. Elemental Ta is seen diffused into the O-rich tissue-material interface revealing dominant Ta_2O_5 presence. b. Schematic representation of surface biochemical mechanisms taking place at a cellular level for the anodized Ti-Ta alloys. Coexisting nanostructured Ti and Ta surface oxide layers accelerate ion interactions in a physiological environment resulting in the formation of an apatite-like layer on the surface of these implants This apatite layer in turn aids in initial protein requirements that serve as the basis for subsequent cell-material interactions.

TABLE 1

Total energy input calculation for LENS™ processed compositions.

Sample	Power (W)	Scan Speed (mm/min)		Hatch Distance (mm)		Layer height (mm)		E (J/mm^3)	
		Dense	Porous	Dense	Porous	Dense	Porous	Dense	Porous
CpTi									
10Ta	342–378	685.8						4.9–5.5	3.0–4.3
25Ta	366–404	508.0	609.6	0.5	0.96	0.2	0.15	7.2–7.9	4.1–4.6
100Ta	409–451	-		-		-		-	4.6–5.1

Mater Today (Kidlington). Author manuscript; available in PMC 2022 May 01.

TABLE 2

Calculations from compression testing. Elastic modulus decreases with an increase in Ta content in Ti. Compressive yield strength increases for 10Ta-P due to the formation of metastable α″ martensite phases, which decreases the further addition of Ta (25Ta-P), resulting in a decrease in compressive yield strength to β-phase stabilization. A sample size of $n = 3$ for each composition was used for individual experiments.

Sample	Ultimate compressive strength (MPa)	0.2%offset Yield strength (MPa)	Elastic Modulus (GPa)
CpTi-P	1220	603 ± 9	127 ± 11
10Ta-P	1310	803 ± 70	79 ± 5
25Ta-P	1180	686 ± 13	64 ± 6
100Ta-P	560	277 ± 2	98 ± 4

TABLE 3

Contact angle and surface energy evaluation of CpTi, 10Ta, and 25Ta surfaces. The contact angle for Dulbecco's Modified Eagle medium (DMEM) on all three surfaces are similar to each other despite 10Ta and 25Ta showing lower surface energy compared to CpTi.

Liquids	CpTi	10Ta	25Ta
DMEM	40 ± 1	42 ± 2	38 ± 1
Di-iodomethane	32 ± 1	36 ± 1	31 ± 2
Ethylene Glycol	28 ± 3	23 ± 2	35 ± 1
Formamide	30 ± 2	32 ± 1	37 ± 2
Surface energy (mJ/m^2)	61 ± 5	47 ± 2	58 ± 5